Journal Name

Optical properties of organic/inorganic perovskite microcrystals through the characterization of Fabry-Pérot resonances[†]

Fernando Ramiro-Manzano,[*a] Rocío García-Aboal,[a] Roberto Fenollosa,[a] Stefano Biasi,[b] Isabelle Rodriguez,[a] Pedro Atienzar,[a] and Francisco Meseguer[a]

The precise knowledge of the optical properties, specifically the refractive index, of organic/inorganic perovskites is essential for pushing forward the performance of the current photovoltaic devices that are being developed from these materials. Here we show a robust method for determining the real and the imaginary part of the refractive index of MAPbBr3 thin films and micrometer size single crystals with planar geometry. The simultaneous fit of both, the optical transmittance and the photoluminescence spectra to theoretical models defines unambiguously the refractive index and the crystal thickness. Because the method relies on the optical resonance phenomenon occurring in these microstructures, it can be used to further develop optical microcavities from perovskites or from other optical materials.

1 Introduction

Organic/Inorganic perovskites have emerged as a new material for cutting edge applications in photon harvesting[1–9] and light emission[10–21]. In a very short period of time we have witnessed extraordinary achievements in the perovskite-rush race for high efficiency solar cells[2,4,9], in spite of the fact that this material suffers of important drawbacks as a poor chemical, thermal and even optical stability, which hampers the development of market devices[22]. In this rich but difficult scenario, one of the key factors for achieving notable improvements is to have an accurate knowledge of the refractive index of the materials, especially at wavelengths near the optical absorption/emission region. In order to determine the wavelength dispersion of the real and imaginary part of this parameter, many researchers make use of different optical techniques like ellipsometry, which is appropriate for macroscopic samples. However, different approaches are required for characterizing micrometer size structures or small crystal domains of an optical material. Such micro or nanostructures (thin films, planar prisms and microwires) show strong interference effects because they behave as optical Fabry-Pérot

type resonators. The resonant response of this kind of cavities has been extensively studied and modelled through their transmittance/reflectance spectra. In fact, it represents the most general case of an optical resonator[23,24]. Also, the interference phenomenon is expected to appear in the photoluminescence spectra[24], but few theoretical modelling studies have arisen in this regard[25,26]. Here we show a method for determining the optical parameters of a micrometer size structure by fitting simultaneously its optical transmittance (OT) and its photoluminescence (PL) spectra. It allows a faithful determination of the real (nr) and the imaginary (ni) components of the refractive index value at a wavelength bandwidth around the optical absorption edge. This results as an in-situ source of information employing common characterization techniques at the microscale, and thus enriching the derived results. In this way this could avoid the use of additional equipment such as commercial ellipsometers and prism couplers. Although we have applied it to the case of perovskite-based microstructures, it can be used for extracting the optical parameters of other materials. For obtaining high fit robustness, the ingredients are: the presence of PL emission and modal structure in the spectra. In order to explain the underlying idea of the method we have used an asymmetrical planar cavity that reproduces faithfully our experimental conditions. In the next section we explain the theoretical model to fit both OT and PL spectra, starting from a simple configuration where only light with k-vector perpendicular to the cavity surface is considered. Then we include the effect of the numerical aperture of the collecting microscope objectives, and analyse the influence of the cavity thickness. Finally, in the results section, several fitted

optical parameters, specially the refractive index values for a perovskite cavity, are shown and compared with other values appearing in the literature, that were obtained by different approaches.

2 Modelling Details

2.1 Optical transmittance and photoluminescence of a Fabry-Pérot cavity at normal incidence/collection

The type of Fabry-Pérot cavity studied here is composed by the active material (AM) constituted by a high refractive index thin film, such as a perovskite single crystal, deposited on a glass substrate. It is an asymmetric cavity because it includes two different dielectric interfaces (SiO_2/AM and AM/air). Figure 1(a) and 1(b) illustrate this configuration and show the schemes utilized for modelling OT and PL measurements respectively. As a first approach, we have assumed that the light wave vector is perpendicular to the front surface of the sample. The fingerprint of such a cavity is a train of peaks produced by the optical resonant modes that appear in the OT (black curve in Figure 1(c)) as well as in the PL spectra (black curve in Figure 1(d)). This optical phenomenon is derived from the light confinement in the AM film through recursive internal reflections at the interfaces (Figure S1). However, in spite of their similar physical origin, the resonant modes in OT and PL spectra show notable differences in their envelope shapes, because they include distinct ingredients that should be taken into account, particularly in the PL spectra as we will see below. In the case of OT, the relation between the incident (E_{in}) and the transmitted (E_{out}) electromagnetic fields follows the well-known relation[23] (see Section S2):

$$\frac{E_{out}}{E_{in}} = \frac{t_{12}t_{23}\sqrt{a}e^{i\beta L}}{1 - ar_{23}r_{21}e^{i\beta 2L}}, \tag{1}$$

where the t_{ij}, r_{ij}, are the transmittance and the internal reflection coefficients of the dielectric interfaces, with $[i, j]$ accounting for the incident and propagating material respectively, i.e. 1 the substrate, 2 the hybrid perovskite and 3 the air, (see Figure 1(a) and (b)), a is an exponential term related to propagation losses ($a = e^{-2k_0 L n_i}$), k_0 is the free space wavenumber ($k_0 = \frac{2\pi}{\lambda_0}$), β is the propagation parameter ($\beta = k_0 n_r$), λ_0 is the free-space wavelength, L is the sample thickness, and n_r and n_i are the real and imaginary part of the refractive index respectively (see Section S1). From the Equation 1, we can derive the optical transmission parameter T,

$$T = \left|\frac{E_{out}}{E_{in}}\right|^2 = \frac{at_{12}^2 t_{23}^2}{a^2 r_{21}^2 r_{23}^2 - 2ar_{23}r_{21}\cos(2\beta L) + 1}. \tag{2}$$

This relation shows local maxima when the cosine term is maximized, that is when $2\beta L = 2\pi m (m = 1, 2, 3, \ldots,)$. Each of them corresponds to a resonance condition with a m-number mode-order. Therefore, they define a sequence of peaks in the spectrum. Figure 1(c) highlights two of those peaks (dotted curves) for modes $m = 38$ and $m = 42$, which have been decomposed from the total spectrum. They have a Lorentzian shape with a Full Width at Half Maximum ($\Delta\lambda_h$) that is modulated by the losses, related to the propagation (a) and the transmission through the interfaces (see SI). The Figure indicates three spectral regions

with ($a = 0.44$), without ($a = 1$) and with intermediate propagation losses, which have been highlighted with red, blue and white background colours respectively. As expected (see Section S4), the $\Delta\lambda_h$ of the resonance occurring at the low losses region ($m = 38$) is substantially smaller than that of the resonance at the high losses region ($m = 42$). The upper (T_+) [blue curve] and lower (T_-) [green curve] bounds, and also the visibility factor (V) of the peaks can be written as:

$$T_\pm = \frac{at_{12}^2 t_{23}^2}{(1 \mp ar_{23}r_{21})^2} \tag{3}$$

and

$$V = \frac{(T_+ - T)_-}{T_+} = \frac{4ar_{23}r_{21}}{(1 + ar_{23}r_{21})^2}. \tag{4}$$

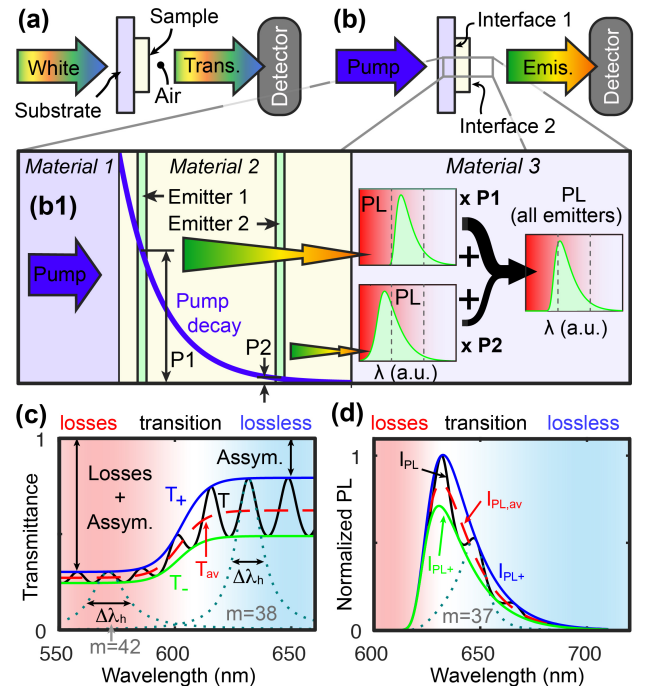Both numerator and denominator of T_+ (see Equation 3) lead

Fig. 1 Schematic representation of the OT (a) and PL (b) experiments. (b1) Effect of the pump and PL propagation losses over the forward PL response. Here, the contributions to the emission of two slices of the active material, excited by P1 and P2 pump intensities, are highlighted. (c) Calculated transmittance (black curve) of an asymmetrical thin film cavity ($r_{12} = 0.2$, $r_{23} = 0.6$, $n_r = 2.4$). Three spectral regions corresponding to three different scenarios, one with moderate propagation losses ($a = 0.44$, red colour background), another one without losses ($a = 1$, blue colour background) and a transition region between them with intermediate losses (white colour background) have been considered. The transmittance T is limited by T_+ (blue line) and T_- (green line). These two limits comprise an average transmission T_{av} (dashed red line). The transmittance offset or penalty from a full transmittance has been indicated by vertical arrows and it is limited by both, the propagation losses and the cavity asymmetry. Two representative Lorentzian peak decompositions are plotted (dotted lines) for the propagation loss ($m = 42$) as well as the lossless ($m = 38$) scenarios (see SI). (d) Similar plot as (c) but for the PL emission. The parameters are the same with the exception of those of the losses region that are more realistic ($n_i = 0.18$, therefore $a \approx 0$). Only a Lorenzian peak in the transition region has been decomposed ($m = 37$). This peak is highly perturbed by the $I_{(PL)}$ envelopes.

to a decrease in transmittance for increasing losses. Also from Equation 3, it is important emphasizing the possibility to reach full transmittance ($T_+ = 1$) values for a propagation lossless ($a = 1$) symmetrical ($r_{21} = r_{23}; t_{12} = t_{23}$) cavity (see Section S2.1). These penalties from achieving full transmittance have been indicated in the Figure 1(c) by vertical arrows in the losses and in the lossless regions. Finally, an average curve T_{av} (dashed red line) could be defined as,

$$T_{av} = \frac{at_{12}^2 t_{23}^2}{1 - a^2 r_{21}^2 r_{23}^2},\tag{5}$$

which describes the integral average of Equation 2 corresponding to the case of rough interfaces, this destroying the Fabry-Pérot resonances.

In the case of the PL spectrum, we show an example of the emission profile taking into account the attenuation through the AM layer of both, the laser pump source and the emitted signal (see Section S4). For understanding this process, Figure 1(b1) shows a simple scheme of the forward emission that corresponds to the most important PL contribution. We can consider the sample is divided into thin slices or sections along the pumping/collection direction. As an example, the Figure shows two slices (Emitter 1 and Emitter 2), which are characterized by being placed at different distances from the AM/air interface, where the collection of light takes place. The emission spectrum of a section consists of a wide bandwidth signal around the absorption edge. However, the blue-side of the emitted light is strongly absorbed when it propagates through the sample because of differences in the absorption with respect to the more transparent red-side of the spectrum. This results in an asymmetrical and red-shifted shaped signal. The position of each emitter determines the light-path length inside the sample, and thus the final red-shift, of its PL contribution. This way, the light from Emitter 1/Emitter 2 will be highly/faintly blue-absorbed, provoking a large/small red-shift respectively of the normalized PL spectra. This absorption process occurs as well for the pumping light, which is monochromatic with $405\,nm$ of wavelength in our case. Its intensity decreases as the distance from the entering interface (substrate/perovskite) increases (blue curve). Therefore, Emitter 1 and Emitter 2 are excited by intensities P1 and P2 respectively. In any case, the resulting spectrum is a superposition of the signals emitted by all the sections, weighted by the pump intensity that excites each of them. Equation 6 summarizes such calculation where resonant effects of the pump signal and photon reemission have been neglected (see Section S4). The first one because of the high absorption at the pumping wavelengths and the second one because of the reduced size of the cavity[4].

$$I_{PL} = \frac{I_E I_P t_{23}^2 t_{12(p)}^2}{a^2 r_{21}^2 r_{23}^2 - 2ar_{23}r_{21}\cos(2\beta L) + 1}.\tag{6}$$

I_E is a term originated from the light emission according to the generalized Planck law:

$$I_E = \frac{2k_0 \xi n_i E_{ph}^2 N_{ph}}{e^{\frac{(E_{ph} - \mu)}{Tk_B}} - 1}\tag{7}$$

and I_P is related to the pump and the emitted signal propagation losses through the perovskite material.

$$I_P = \frac{a}{2}\left(r_{21}^2 \frac{1 - e^{-2L\left(k_{0(p)}n_{i(p)} + k_0 n_i\right)}}{k_{0(p)}n_{i(p)} + k_0 n_i} + \frac{1 - e^{-2L\left(k_{0(p)}n_{i(p)} - k_0 n_i\right)}}{k_{0(p)}n_{i(p)} - k_0 n_i}\right).\tag{8}$$

In these Equations, $k_{0(p)}$, $t_{12(p)}$ and $n_{i(p)}$ account for the free space wavenumber, the transmission coefficient and the complex part of the refractive index for the pump signal respectively, ξ is related to the photogeneration efficiency, N_{ph} corresponds to the number of pumping photons, E_{ph} is the emitted photons energy, μ is the chemical potential, k_B is the Boltzman constant and T is the sample temperature[25,26] (see Section S4). In a similar manner as the OT in Equation 2, the PL formula has the same oscillatory term ($a^2 r_{21}^2 r_{23}^2 - 2r_{23}(ar_{21})\cos(2\beta L) + 1$). Therefore both, the PL and the OT spectra keep the same interference ingredients but with different envelopes. We can also define for the PL spectra three different spectral regions [see Figure 1(d)], one with losses ($a \approx 0$, red colour background) where in principle the resonant modes widen and finally disappear, followed by a transition zone (white colour background) where resonances are visible (see for instance the Lorentzian peak (dotted line) associated to a mode with order $m = 37$) and finally a lossless region ($a \approx 1$, blue colour background) where the PL and their peaks disappear. We can also derive similar expressions for the upper I_{PL+} (blue curve) and lower I_{PL-} (green curve) bounds of the emission as well as for the average PL signal $I_{PL,av}$ (dashed red curve), this time restricted to the wavelength region of the light emission,

$$I_{PL\pm} = \frac{I_E I_P t_{23}^2 t_{12(p)}^2}{(1 \mp ar_{23}r_{21})^2}\tag{9}$$

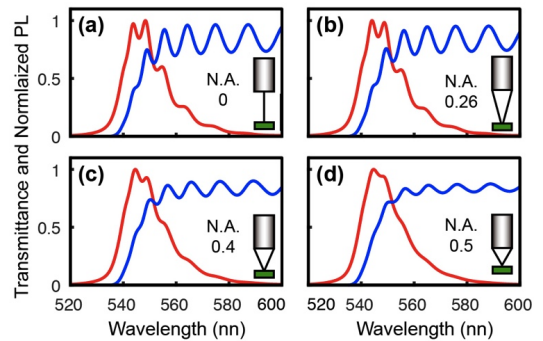$$I_{PL,av} = \frac{I_E I_P t_{23}^2 t_{12(p)}^2}{1 - a^2 r_{21}^2 r_{23}^2}.\tag{10}$$

Fig. 2 Transmittance (blue line) and Normalized PL (red line) spectra for different objectives: N.A. 0 (a), N.A. 0.26 (b), N.A. 0.4 (c), N.A. 0.5 (d) for a perovskite layer of $3.96\ \mu$m thick. The refractive index and extinction dispersion have been extracted from the fit of experimental data (see Figure 4).
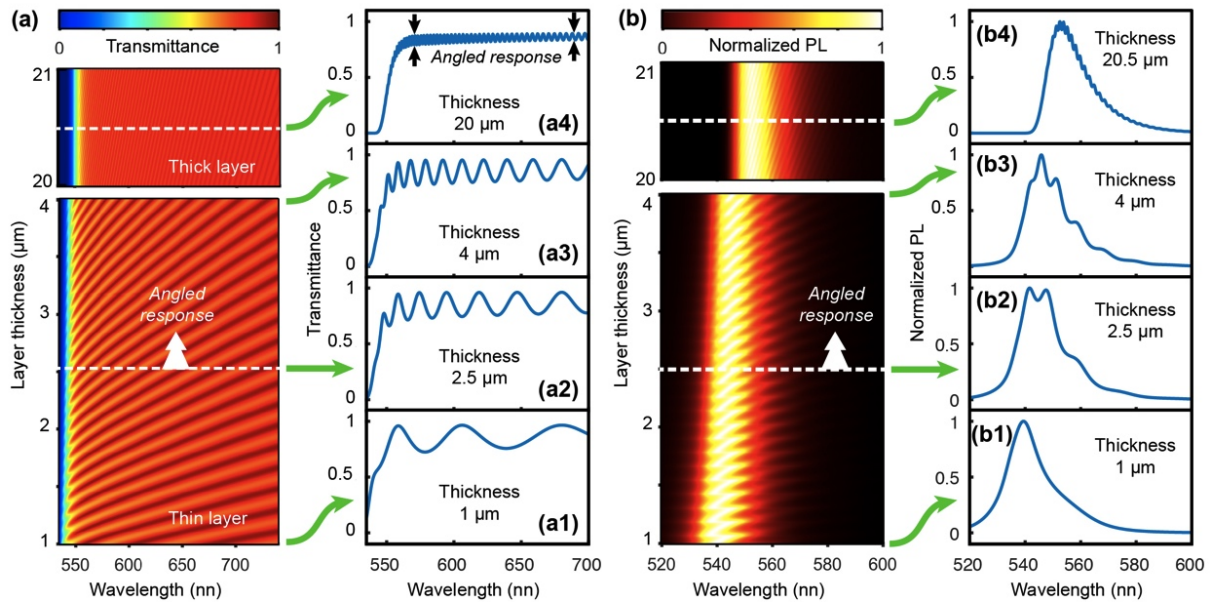
Fig. 3 Calculated (a) Transmittance and (b) Normalized PL spectra of a *MAPbBr3* thin film as a function of the layer thickness for a collection objective of N.A.= 0.26 where (a1)-(a4) and (b1)-(b4) represent respectively 1, 2.5, 4 and 20.5 μm sample thickness. The refractive index and extinction dispersion have been extracted from the fit of experimental data (see Figure 4).

2.2 Effect of the collection cone

Collection lenses allow magnifying optical signal by collecting light coming from different k-vector angles. The higher the numerical aperture (N.A.) of a lens, the larger the range of collected k-vector angles. In this way, the enlargement of the collecting angle leads to an increment in the number of wave components of the Fabry-Pérot resonances (see Sections S2-S4), and it can blur the visibility of the peaks, as shown in Figure 2. In general, the resonances appear much more pronounced in the OT spectrum than in the corresponding PL spectrum because of their different envelope curves, flat and with a pronounced slope respectively, around the wavelength region where absorption losses vanish. Therefore, the increase of the N.A. of the collection lens produces a more drastic effect in the PL spectra, where the train of peaks may even disappear for some cases. Figures 2(a)-(d) represent different scenarios for different collection cones, for a 3.96 μm-thick perovskite layer that corresponds to the characterized sample in the Section 3. Since changing a particular collection angle from the normal direction is equivalent to increase the sample thickness, here the effect of the N.A. was calculated by averaging Equation 2 and 6 for OT and PL spectra respectively for several values of an effective thickness ($L/cos(\theta_r)$), where θ_r varies from 0 to the limit refractive angle inside the perovskite layer. This limit angle can be easily calculated from the N.A. and the Snell law at each wavelength value. In the case of the r and t parameters, their values are marginally affected by θ_r because the refracted angle is much lower than the collection angle. A N.A.$\leq$ 0.26 influences marginally the peak contrast for thin cavities as we will see in the next section. Thus a regime of normal incidence/collection could be assumed in those cases. However, in general the effect of the collecting objectives should be considered in the model for N.A.$\geq$ 0.4. As it will be explained in the following paragraphs, the

conjunction of the numerical aperture with the sample thickness plays a pivoting role in the observation of cavity peaks.

2.3 Influence of the film thickness

The thickness of a Fabry-Pérot cavity influences strongly the peak visibility. Figure 3 shows contour-plot stacks of the OT (a) and the PL (b) response of a *MAPbBr3* perovskite thin film type cavity as a function of wavelength and thickness. We used the refractive index for this material (both real and imaginary values) obtained by the fitting process detailed in the following section, and we assumed a N.A.= 0.26 for the collection objective. Each oblique line accounts for a resonant mode m. This could be easily understood by examining the resonant condition, which is a simple line Equation: $L = \frac{m \cdot \lambda_0}{2n_r}$, whose slope depends on the mode order and the refractive index. The lack of a constant term in this first order polynomial form indicates that the m-lines start from a hypothetical wavelength origin. In the case of the OT, these m-lines extend over the large transparent region (red area in Figure 3(a)). However, they appear only within the bandwidth of the PL signal [Figure 3(b)]. It is worth underlining several properties of these contour-plots: (i) a horizontal cross section for a given thickness corresponds to the spectrum of a cavity with such a thickness value [Figures (a1-a4) for OT, and Figures (b1-b4) for PL]. (ii) each spectrum intercepts several m-lines depending on the layer thickness, the thicker the layer or the shorter the wavelength, the higher the density of such interceptions. This explains the behaviour of the free spectral range (FSR), which corresponds to the distance between successive Fabry-Pérot peaks (see Section S5), (iii) a larger refractive index value n_r means a smaller m-line slope that results in an increase of the density of m-lines in any spectrum. The fact of assuming a finite N.A. in the calculations can be appreciated by considering the visibility and contrast of the

interference peaks in Figure 3 (a1)-(a4). While these parameters are independent of the sample thickness at normal incidence in the region where absorption vanishes (see Equation 4), they are now reduced when layer thickness L and λ increases. The latter dependence is subtle, but it appears clearer in Figure 3 (a4). In fact, the thicker the sample the closer the m-lines (the smaller the FSR), and consequently the more pronounced are the effects of the numerical aperture because each angular component of the collection cone is described by an effective increase of the sample thickness ($L/cos(\theta_r)$). On the other hand, the increase of the slope of the m-lines at shorter wavelengths yields more similar angular components, thus reducing their influence in the N.A.

Finally is worth emphasising that sample thickness also changes both the peak position as well as the asymmetry of the PL background profile (see Figures 3(b1)-(b4)) because the optical-path length determines the attenuation of the blue-side of the emitted signal.

3   Results and Discussion

OT and PL spectra of perovskite optical-microcavities single-crystals (Figure 4(a)) could be successfully fitted to those models that have been detailed in previous sections. Figure 4 (b) and (c) show experimental (black) and fitted (red) curves corresponding to OT and PL spectra respectively of a 3.96 μm thick *MAPbBr*3 crystal deposited on a glass substrate. The thickness value was obtained from the fitting process itself. Besides Equation 2 and 6, other important ingredients of the fitting procedure are i) the use of polynomials, Sellmeier and Sigmoid curves for parametrizing the refractive index, ii) the N.A. of the collecting objective, 0.4 in our case, and iii) the fact that the fitting process is performed simultaneously for both OT and PL spectra. This helps disregarding spurious solutions and strengthens the reliability in the fitted parameters. Figures 4(d) and 4(e) show the fitted values (dark brown curves) of the real and imaginary part respectively of the refractive index. They resemble other values reported in the literature, particularly those of J.-S. Park et al.[27] (blue curves) that were obtained by the ellipsometry technique. Here, the differences could be attributed not only to the distinct measurement method but also to different sample fabrication processes[28]. It is interesting to investigate the performance of the perovskite crystal as optical cavity through the Finesse (F) and the Quality Factor (Q) of its optical resonant modes, identified by their mode-order, m, (highlighted on top of each resonance peak in Figure 4(b) and (c)). These parameters are proportional to the amplification of light inside the crystal and to the peak isolation in the case of F, and cavity lifetime in the case of Q[23,24] (see Section S5). Therefore, high F and Q values are desired for large light-matter interactions. In the present case of the perovskite crystal, the maximum values for F (≈ 0.95) and Q (≈ 80.1) appear for modes $m = 32$ and $m = 33$ (see Figure 4(f) and 4(g) respectively), that are near the absorbance edge, where the refractive index is high and the losses are moderate (see Section S6). The development of future cutting edge applications in this area would require the improvement of these important parameters. This could be achieved for example by shaping the perovskite material in more effective geometries such as circular, spherical or photonic crystal

(see Section S7). A high improvement of the cavity could help to boost, deepen into or discover new excellent or exotic properties of this material[29,30]. We think this constitutes a very interesting research branch for the future.
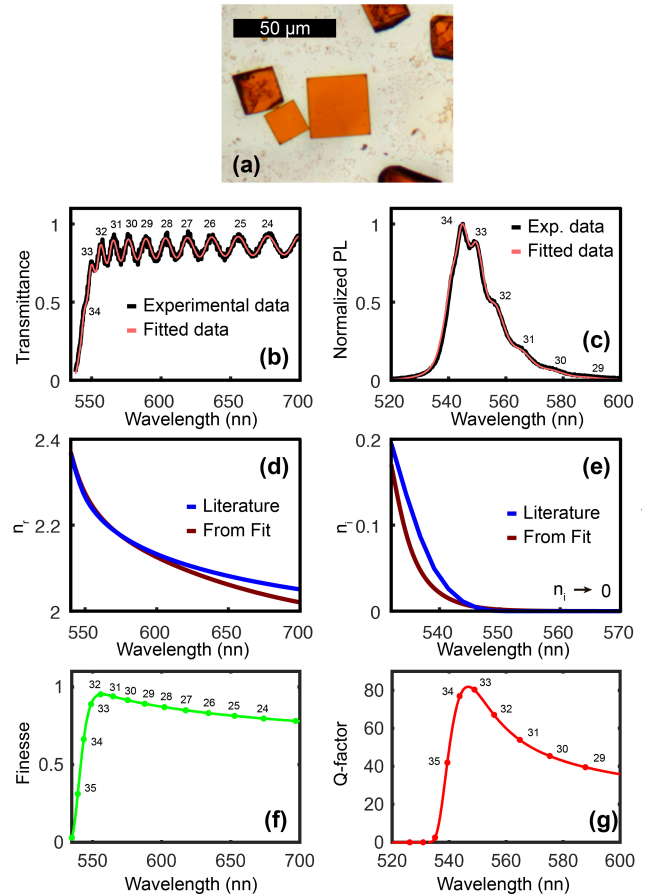

Fig. 4 (a) Optical microscopy image of the measured *MAPbBr*3 crystal microcavity (square structure at the center of the image). (b) and (c) Experimental data and fitted curves for the OT and the PL spectra respectively. Resonant modes are indicated on top of their resonance peak by their mode-order, m. (d) Real and (e) imaginary part of the fitted refractive index and that of ref[27] for comparison. (e) Finesse and (f) Quality Factor for all of the identified modes. The lines are to guide the eye.

4   Experimental Section

Micrometer size single crystals of *MAPbBr*3 were synthesized from a precursor solution composed by methylammonium bromide (*MABr*) 1M and lead bromide (*PbBr*2) 1M in N, N-dimethylformamide (*DMF*), and N-cyclohexyl-2-pyrrolidone (*CHP*) as additive. The *MAPbBr*3 crystals were grown onto quartz substrates by spin-coating the precursor solution at 800 rpm at room temperature. The samples were annealed at $90°C$ during 2 minutes to remove the solvents and complete the crystallization process[31]. Then, the crystals were characterized by X-ray diffraction (*XRD*) and ultraviolet-visible spectrophotometry (UV-Vis)[32] (see Section S8). The optical setup for measuring the OT and PL spectra[31] consists of a microscope-based characterization system where the input signal is generated from either, a tungsten lamp (for transmission characterization) or a solid state 404 nm

laser (for PL characterization) passing though a 20x 0.4 N.A. objective illuminating the sample with 0.1 mW of optical power. The sample is placed in a 3-axis positioning stage for selecting the target planar microcrystal cavity. The output signal is collected with another objective with the same features, and then the light is focused in a pinhole for selecting a target area inside the sample. This permits to avoid any perturbation from the borders and to study faithfully the transmission spectrum by subtracting the AM transmitted intensity from a background signal, acquired from a void area. Finally, the light matches a spectrometer and the signal is detected by a nitrogen-cooled CCD array. The experimental data fitting has been performed by employing the mathematical commercial package Matlab.

5 Conclusions

We have shown a simple procedure to extract accurately both the real and the imaginary part of the refractive index in a wide wavelength region around the electronic band gap, and the thickness of a *MAPbBr*3 single-crystal placed on a silica substrate. The method consists in a dual fit of the Transmittance and the Photoluminescence spectra to analytical models. Both spectra show Fabry-Pérot oscillations corresponding to resonant modes with different envelopes. We have analysed how the parameters of the models and other external factors such as the numerical aperture of the collecting lenses influence the final shape of the resonances. At the same time, the models constitute a guide for finding the conditions for a thin film type microstructure to have an optical cavity response. The extracted information from an isolated single crystal could be useful for understanding or improving the macroscopic behavior of polycrystalline materials, where crucial information, such as the described resonant phenomena, could be hidden behind the collective contribution to the material response.

Conflicts of interest

There are no conflicts to declare.

Acknowledgements

Notes and references

1 J.-H. Im, C.-R. Lee, J.-W. Lee, S.-W. Park and N.-G. Park, *Nanoscale*, 2011, **3**, 4088–4093.

2 M. M. Lee, J. Teuscher, T. Miyasaka, T. N. Murakami and H. J. Snaith, *Science*, 2012, **338**, 643–647.

3 M. Liu, M. B. Johnston and H. J. Snaith, *Nature*, 2013, **501**, 395.

4 L. M. Pazos-Outón, M. Szumilo, R. Lamboll, J. M. Richter, M. Crespo-Quesada, M. Abdi-Jalebi, H. J. Beeson, M. Vrućinić, M. Alsari, H. J. Snaith, B. Ehrler, R. H. Friend and F. Deschler, *Science*, 2016, **351**, 1430–1433.

5 N. J. Jeon, J. H. Noh, W. S. Yang, Y. C. Kim, S. Ryu, J. Seo and S. I. Seok, *Nature*, 2015, **517**, 476.

6 J. Burschka, N. Pellet, S.-J. Moon, R. Humphry-Baker, P. Gao, M. K. Nazeeruddin and M. Grätzel, *Nature*, 2013, **499**, 316.

7 A. Kojima, K. Teshima, Y. Shirai and T. Miyasaka, *Journal of the American Chemical Society*, 2009, **131**, 6050–6051.

8 H.-S. Kim, C.-R. Lee, J.-H. Im, K.-B. Lee, T. Moehl, A. Marchioro, S.-J. Moon, R. Humphry-Baker, J.-H. Yum, J. E. Moser, M. Grätzel and N.-G. Park, *Scientific Reports*, 2012, **2**, 591.

9 W. S. Yang, B.-W. Park, E. H. Jung, N. J. Jeon, Y. C. Kim, D. U. Lee, S. S. Shin, J. Seo, E. K. Kim, J. H. Noh and S. I. Seok, *Science*, 2017, **356**, 1376–1379.

10 H. Cho, S.-H. Jeong, M.-H. Park, Y.-H. Kim, C. Wolf, C.-L. Lee, J. H. Heo, A. Sadhanala, N. Myoung, S. Yoo, S. H. Im, R. H. Friend and T.-W. Lee, *Science*, 2015, **350**, 1222–1225.

11 Z.-K. Tan, R. S. Moghaddam, M. L. Lai, P. Docampo, R. Higler, F. Deschler, M. Price, A. Sadhanala, L. M. Pazos, D. Credgington, F. Hanusch, T. Bein, H. J. Snaith and R. H. Friend, *Nature Nanotechnology*, 2014, **9**, 687.

12 Y.-H. Kim, H. Cho, J. H. Heo, T.-S. Kim, N. Myoung, C.-L. Lee, S. H. Im and T.-W. Lee, *Advanced Materials*, **27**, 2015, 1248–1254.

13 R. L. Z. Hoye, M. R. Chua, K. P. Musselman, G. Li, M.-L. Lai, Z.-K. Tan, N. C. Greenham, J. L. MacManus-Driscoll, R. H. Friend and D. Credgington, *Advanced Materials*, **27**, 2015, 1414–1419.

14 N. K. Kumawat, A. Dey, K. L. Narasimhan and D. Kabra, *ACS Photonics*, 2015, **2**, 349–354.

15 G. Li, Z.-K. Tan, D. Di, M. L. Lai, L. Jiang, J. H.-W. Lim, R. H. Friend and N. C. Greenham, *Nano Letters*, 2015, **15**, 2640–2644.

16 J. Wang, N. Wang, Y. Jin, J. Si, Z.-K. Tan, H. Du, L. Cheng, X. Dai, S. Bai, H. He, Z. Ye, M. L. Lai, R. H. Friend and W. Huang, *Advanced Materials*, **27**, 2015, 2311–2316.

17 A. Sadhanala, A. Kumar, S. Pathak, A. Rao, U. Steiner, N. C. Greenham, H. J. Snaith and R. H. Friend, *Advanced Electronic Materials*, 2015, **1**, 1500008.

18 J. C. Yu, D. B. Kim, G. Baek, B. R. Lee, E. D. Jung, S. Lee, J. H. Chu, D.-K. Lee, K. J. Choi, S. Cho and M. H. Song, *Advanced Materials*, 2015, **27**, 3492–3500.

19 N. K. Kumawat, A. Dey, A. Kumar, S. P. Gopinathan, K. L. Narasimhan and D. Kabra, *ACS Applied Materials & Interfaces*, 2015, **7**, 13119–13124.

20 O. A. Jaramillo-Quintero, R. S. Sanchez, M. Rincon and I. Mora-Sero, *The Journal of Physical Chemistry Letters*, 2015, **6**, 1883–1890.

21 H. Zhu, Y. Fu, F. Meng, X. Wu, Z. Gong, Q. Ding, M. V. Gustafsson, M. T. Trinh, S. Jin and X.-Y. Zhu, *Nature Materials*, 2015, **14**, 636.

22 M. Lira-Cantu, *Nature Energy*, 2017, **2**, 17115.

23 A. Yariv and P. Yeh, *Optical Electronics in Modern Communications*, 2007.

24 B. Saleh and M. Teich, *Fundamentals of Photonics* 2007.

25 S. Knabe, M. Langemeyer, F. Heidemann, R. Brüggemann and

G. H. Bauer, *Progress in Photovoltaics: Research and Applications*, 2011, **19**, 927–936.

26 O. Neumann, R. Brüggemann, N. Könne and G. H. Bauer, *physica status solidi (a)*, 2014, **211**, 1128–1133.

27 J.-S. Park, S. Choi, Y. Yan, Y. Yang, J. M. Luther, S.-H. Wei, P. Parilla and K. Zhu, *The Journal of Physical Chemistry Letters*, 2015, **6**, 4304–4308.

28 M. E. Calvo, *J. Mater. Chem. A*, 2017, **5**, 20561–20578.

29 H. Tahara, T. Aharen, A. Wakamiya and Y. Kanemitsu, *Advanced Optical Materials*, 2018, **6**.

30 T. Handa, H. Tahara, T. Aharen and Y. Kanemitsu, *Science Advances*, 2019, **5**.

31 R. García-Aboal, R. Fenollosa, F. Ramiro-Manzano, I. Rodríguez, F. Meseguer and P. Atienzar, *ACS Omega*, 2018, **3**, 5229–5236.

32 J. H. Heo, D. H. Song and S. H. Im, *Advanced Materials*, 2014, **26**, 8179–8183.